Int J Adv Manuf Technol (2015) 81:563–576
DOI 10.1007/s00170-015-7234-8

ORIGINAL ARTICLE

The influence of laser welding configuration on the properties of dissimilar stainless steel welds

L. Romoli[1] **· C. A. A. Rashed**[2]

Received: 8 January 2015 / Accepted: 26 April 2015 / Published online: 10 May 2015

Abstract Laser beam welding of dissimilar ferritic/martensitic stainless steels was performed in constrained butt joint configuration with the objective of identifying the influence of the melting ratio between the two base metals on the ultimate shear strength of the welds. Based on a full factorial design, experiments demonstrated that varying the incidence angle up to 45° and offsetting the focal position with respect to the materials' interface within the limits imposed by the laser spot diameter are a reliable method to control the melting ratio and maintaining the expected resistance length at the material interface. The weld configuration parameters were correlated by means of the analysis of variance (ANOVA) method with shear resistance length and the melting ratio: the incidence of surface cracks can be significantly reduced increasing the ferritic steel area, involved in the formation of seam, over 60 % of the whole melt zone. Push-out tests performed on the specimens revealed that such a configuration has beneficial aspects on the ultimate shear strength of the seam meaning that the prevailing effect is the decreased brittleness of the weld by decreasing its carbon content under 0.5 % in weight.

Keywords Laser welding · Dissimilar steels · Melting ratio

1 Introduction

The recent advancement in manufacturing technology is increasing the demand for dissimilar metal welding. Joints between components of different material or compositions are commonly used in the power generation, chemical, petrochemical, nuclear, automobiles, and electronics industries [1]. The ability to use different metals and compositions in a product provides the designer and production engineer with greater flexibility and often results in technical and economic advantages over components manufactured from a single material. Many problems are also associated to the topic of dissimilar welding, depending on the metals being joined and the process employed. In the welding of dissimilar metals, the different chemical, metallurgical, and physical properties such as thermal conductivity, thermal expansion coefficient, and melting point should be taken into consideration [2]. The formation of detrimental metallurgical phases in these welds could result in decrease in mechanical and functional properties of the joint. The difference between the physical properties of the two metals to be welded leads to an asymmetry in heat and fluid flow which in turn directs to the development of unique features in the weld microstructure [3]. Thus, solidification microstructures, the asymmetric shape of the weld, and mixing patterns need special attention. Among the available welding techniques, laser welding (high specific power and low-energy input process) is emerging as a valid and promising alternative for joining of dissimilar metal, as it provides solutions to a number of problems encountered with conventional techniques [4].

Laser welding provides several advantages, such as higher productivity, better weld quality with narrow heat-affected zone (HAZ), lower distortions, and higher flexibility over the conventional processes [5]. The weld quality mainly depends on the mechanical properties, weld bead geometry, and

---

✉ L. Romoli
luca.romoli@unipr.it

[1] Department of Industrial Engineering, University of Parma, Parma, Italy

[2] Department of Industrial and Production Engineering, Shahjalal University of Science and Technology, Shahjalal, Bangladesh

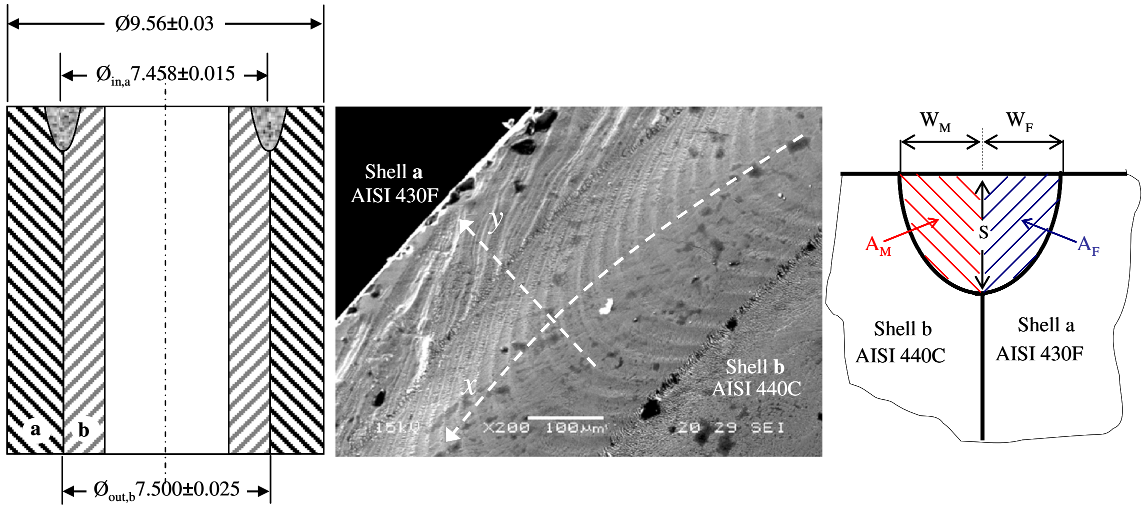

(a) (b) (c)

Fig. 1 **a** Draft of a typical axial section of the welded components with relative dimensions. **b** Top SEM view of a dissimilar butt welded surface at the intersection of AISI 430F and AISI 440C: *x*-axis is circular and set at the material interface, and *y*-axis is positive in the direction of AISI 430F. **c** Theoretical weld bead profile and its geometrical features (W_M: martensitic weld width, W_F: ferritic weld width, *S*: resistance length) together with the areas of both material intersected by the weld (A_M: supposed martensitic weld area, A_F: supposed ferritic weld area)

distortion of the welded joint. All of these quality characteristics are directly related to welding parameters. Several efforts have been done to understand the mechanical and microstructural behavior of dissimilar metal welds and to optimize the welding processes used.

Phanikumar et al. [3] investigated the continuous welding of iron and copper using a laser heat source. The microstructural analysis at different process conditions of the weld/base-metal interface shows features that are different on the two sides of the weld. Vaidya et al. [6] used Nd:YAG laser for dissimilar butt welding of aluminum AA6056 and titanium Ti6Al4V alloy without using a filling wire. In their study, the interfacial area was decreased that resulted in decreased reaction zone, improved interfacial binding, reduced the grain size in the fusion zone, no segregation of grain boundary, and refined microstructure with improved properties. Homogeneous microstructure of the weld metal and very few weld defects were observed in butt welding of two different thickness stainless steel plates [7].

Caiazzo et al. [8] studied the autogenous disk laser welding of dissimilar metals commonly used in aerospace applications. They provided a comprehensive description of the quality issues in terms of both structure and shape defects, via nondestructive tests and dimensional checks by optimizing three factor experimental plans with power, welding speed, and beam angle. Gao et al. [9] developed the laser keyhole welding of titanium and magnesium alloys and showed that the offset, i.e., the change of incident laser beam position, plays the significant role on joint properties by the change of the power density irradiated at the Ti–Mg initial interface. However, the variation of the beam position was not found to be a less significant factor for the weld geometry in keyhole mode of dissimilar austenitic-martensitic stainless steel [10].

Table 1 Average chemical composition of AISI 440C and AISI 430F steels

	%C	%Mn	%Si	%Cr	%S	%Mo
AISI 440C	0.95-1.2	1.00	1.00	16.0–18.0	Max 0.03	0.6
AISI 430F	0.12	1.25	1.00	16.0–18.0	Min 0.15	0.75

The attention paid by researchers on the weld geometry testifies its influence on the mechanical properties of the welded joints and, consequently, on the related welding quality. Liao et al. [11] studied the effects of pulse energy and incident angle on the cross-sectional size and shape of the welded bead. Their study illustrated that laser incidence angle along with the laser energy is an important parameter for controlling the geometry of the welded spot.

Weld material, joint configuration, and welding parameters have significant effects on the weld seam characteristics, on the weld microstructure, on the presence of defects, and on the effective mechanical properties of the whole joint. To optimize the welding parameters and to obtain proper welding geometry, various methods of obtaining the desired output variables throughout model development can be used. Among these, design of experiment (DOE) may be the most efficient way for a systematic study as it grown rapidly by its diversified application in different areas of manufacturing. Benyounis and Olabi [12] reported a literature review

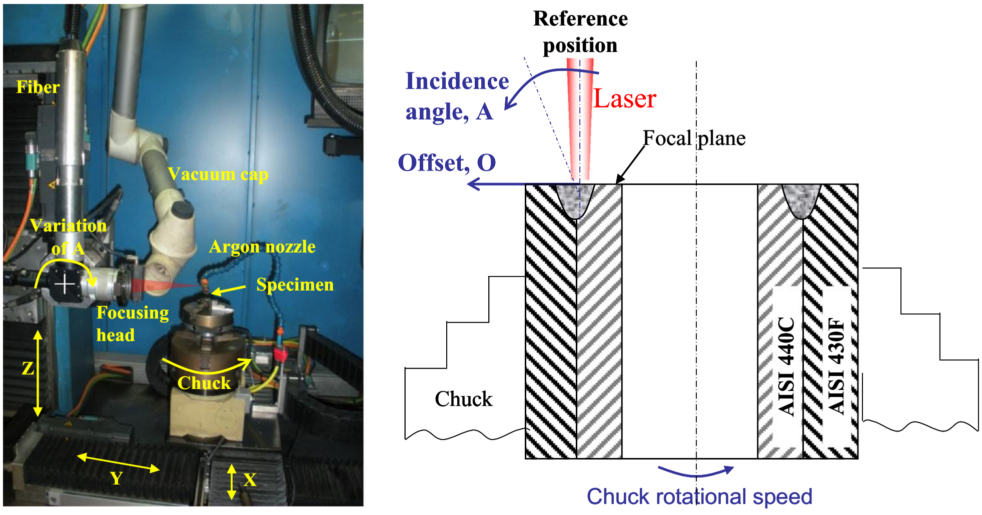

(a) (b)

Fig. 2 **a** Photographic view of Nd:YAG laser welding system. **b** Cross section of the joined components: welding configuration varies from the reference position (beam axis orthogonal to the surface, pointing the intersection of AISI 430F and AISI 440C) with the use of input parameters

on various optimization methods; those are applied to define the desired output variables through developing mathematical models. Anawa and Olabi [13] showed that ferritic/austenitic welded joints have better mechanical properties compared to base metals by the minimization of laser power and maximization of welding speed by the application of the Taguchi approach. Ruggiero et al. [14] optimized the weld bead geometry and investigated the effect of laser power, welding speed, and focal point position on the operating cost using response surface methodology (RSM). Khan et al. [15] also used RSM to optimize the welding parameters (welding speed, laser power, laser incidence angle, and defocus distance) in ferritic/austenitic stainless steel to obtain the most desirable weld quality in terms of weld bead geometry under predefined mechanical strength requirements.

The laser welding mode (conduction or keyhole) affects the size of the fusion zone, as the dilution between two base metals strongly depends on the laser energy supply to the materials. Marashi et al. [16] showed that the failure behavior of the fusion zone of dissimilar stainless steel is controlled by the dilution between two base metals. Dissimilar welding of low carbon to austenitic stainless steel sheets resulted in asymmetric shape of the fusion zone as different materials having different thermal conductivities [17].

From the above literature, it is clear that laser welding is a suitable technique for joining dissimilar metals and explains the reasons of its increasing use also in the field of thin-walled pressure vessels for biomedical and automotive applications [18]. Indeed, high-strength metal cylinders can be capped with a dissimilar metal of various shapes to increase the corrosion properties of the component (e.g., in surgery devices) or to enhance the wear resistance (e.g., parts of valves for precision mechanics), etc.

The extremely precise and intense energy concentration obtainable by modern fiber sources allows for numerous weld configurations at the metal interface. Among all, butt welding is the one which enables an easier control of the mixing between the two dissimilar steels in the melt pool [19].

Table 2 Technical specification of the laser welding process

Laser source	Fiber laser
Laser power (W)	800
Fiber diameter (mm)	0.4
Collimating (mm)	200
Focusing (mm)	200
Welding speed (mm/s)	65
Shielding gas type	Argon
Shielding gas flow rate (l/min)	6

Table 3 Experimental conditions and response factors

Process factors	Tested values			
O offset (μm)	0	100	200	
A incidence angle (°)	0	15	30	45
Constant factors				
Base material	Outer shell	AISI 430F		
	Inner shell	AISI 440C		
Response factors				
Weld bead characteristics	Resistance length (*S*)			
	Melting ratio (MR)			

Table 4 Design matrix with actual factors and measured mean responses

Standard order	Process factors		Response factors	
	O (μm)	A (deg)	MR (a.u.)	S (μm)
1	0	0	0.8	760
2	100	0	2.0	695
3	200	0	2.7	465
4	0	15	0.5	535
5	100	15	1.6	610
6	200	15	2.2	450
7	0	30	0.3	480
8	100	30	0.6	550
9	200	30	1.5	590
10	0	45	0.1	280
11	100	45	0.3	415
12	200	45	0.6	455

Main purpose of the present research is, in fact, to go beyond the already studied influence of process parameters on the weld bead and, then, to identify a reproducible setup for a common laser welding cell to control the melting ratio between two parent metals. The effects of welding parameters like laser beam position (with respect to the materials' interface) and incidence angle (with respect to the materials' irradiated surface) on the weld profile will be studied by means of a structured DOEs. An attempt based on full factorial design will be proposed to mathematically link the parameters determining the butt welding configuration with the geometry of the melt pool and the melting ratio of two dissimilar metals. This step is retained a technical key factor to determine how mixing two different materials could enhance the mechanical properties of the single base metals in butt-welded joints. At this purpose, the final objective is to perform disassembly tests on the obtained joints in order to detect the influence of melting ratio on the ultimate shear strength of the welds.

2 Materials and experimental procedures

2.1 Materials and weld design

Experiments are performed in butt constrained circular seam to replicate the weld configuration of a pressure vessel. The draft in Fig. 1a shows the welding configuration together with the specimens' diameters and their coupling. The internal tubular shell is made of martensitic stainless steel AISI 440C (prehardened and tempered) and is assembled with the external one made of ferritic stainless steel AISI 430F (cold drawn, annealed, and centerless ground). The selected materials are frequently used both in automotive and biomedical applications according to peculiar design criteria which impose high hardness and good resistance to corrosion as well. Table 1 reports the chemical composition of the used steels.

The inside diameter of the outer shell and the outside diameter of the seat are machined to Ø7.500±0.025 mm and Ø7.458±0.015 mm, respectively, to have a clearance fit between them when the shells are assembled.

The geometrical features characterizing the weld seam profile are defined in Fig. 1: W_M represents the weld width on the martensitic material while W_F represents the one on the ferritic stainless steel. The ultimate shear strength of the weld is guaranteed by the length of the melt pool at the material interface, here defined as resistance length S, since the joint is supposed to fail under the action of disassembly forces parallel to the shells' axis.

In order to consider only the influence of the welding configuration on the melt pool geometry and its composition (between the dissimilar steels), the weld seams obtained in this study are performed with the following laser parameters: laser power of 800 W, welding speed of 65 mm/s, and spot diameter of 0.4 mm. This combination results in an energy density (ED calculated as the ratio between the input power and the product of welding speed and spot diameter) supply to the specimen of about 30 J/mm^2. Nevertheless, the findings of this research can be also applied to different combinations of laser

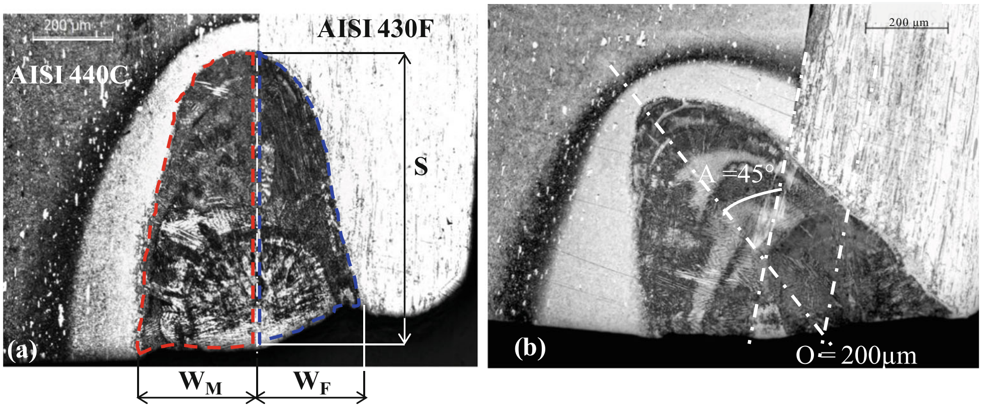

Fig. 3 Cross sections of welds in **a** reference position O=0, A=0° and **b** O=200 μm, A=45°. Cross section (**a**) reports the martensitic area A_M inside the *red-dashed contour* and the ferritic area A_F inside the *blue-dashed contour*

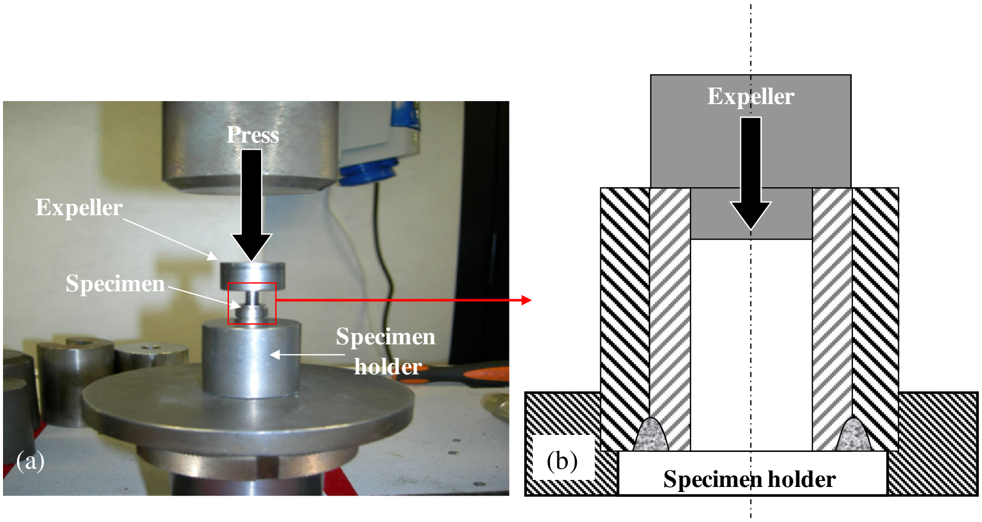

Fig. 4 **a** View of the experimental setup for the push-out test of the weld. **b** Cross-sectional draft of the specimen

parameters under the condition that the heat transfer is conduction dominated (up to 50–60 J/mm^2 according to [20]). Heat exchanges established under the formation of a plasma channel (as in keyhole welding mode) produce much higher thermal transients, thus generating a remarkably different microstructure of the weld with respect to those observable when the weld is conduction dominated.

However, even using low values of ED supply on the steels, the experimental practice often reports the occurrence of microcracks on the seam. These defects are supposed to grow up during the solidification process in zones where the mixing of the two metals with different chemical composition and thermal properties is less homogeneous. Microcracks can be classified according to the ISO 13919-1:1996 [21] standard.

Table 5 Occurrence of surface microcracks on the weld seam with respect to the analyzed weld geometries

Welding configuration	Offset, O (μm)	Incidence angle, A (°)	Surface cracks[a]
1	0	0	1
2	100	0	0
3	200	0	0
4	0	15	3
5	100	15	0
6	200	15	0
7	0	30	3
8	100	30	2
9	200	30	0
10	0	45	3
11	100	45	3
12	200	45	2

Values are attributed according to ISO 13919-1:1996 [17], after inspection on the three samples for each configuration

[a] 0=no defects, 1=exist but acceptable, 2–3=not acceptable

To reduce the incidence of crack formation, which testifies the embrittlement of the weld seam and mostly develops on the side of the martensitic steel, it is here hypothesized to change the position of the laser beam toward the ferritic steel, by offsetting the beam axis with respect to the interface of the two materials.

Nevertheless, increasing the beam offset O (along y-axis in Figs. 1b and 2b) may result in a drastic decrease of the resistance length (up to the value for which the melt pool does not involve the martensitic steel) with a consequent decay in the ultimate shear strength. To avoid this severe limitation and, at the same time, to obtain a weld profile less prone to cracking, the beam incidence angle A (see Fig. 2b) has to be varied as well. This results in the need of defining weld cross-sectional geometries for each combination (O; A) adopted.

Inclining the laser beam has a further beneficial effect of increasing the irradiated area which becomes elliptical (increasing A) with the longer axis disposed along y-direction. The elongation of the irradiated area allows for a reduction of the thermal gradient in y-direction which may contribute to a less severe thermal cycle on the extinction zones of the weld bead, where microcracks usually appear.

For each combination of (O; A), the melting ratio between the two dissimilar steels is supposed to vary, thus influencing the microstructural properties of the weld bead and the occurrence of surface cracking, as also stated in [22]. The melting ratio can be defined by analyzing the cross section of the welds as the ratio between the areas of ferrite and martensite involved in the melt pool, as shown in Eq. (1):

$$\mathrm{MR} = \frac{A_\mathrm{F}}{A_\mathrm{M}} \tag{1}$$

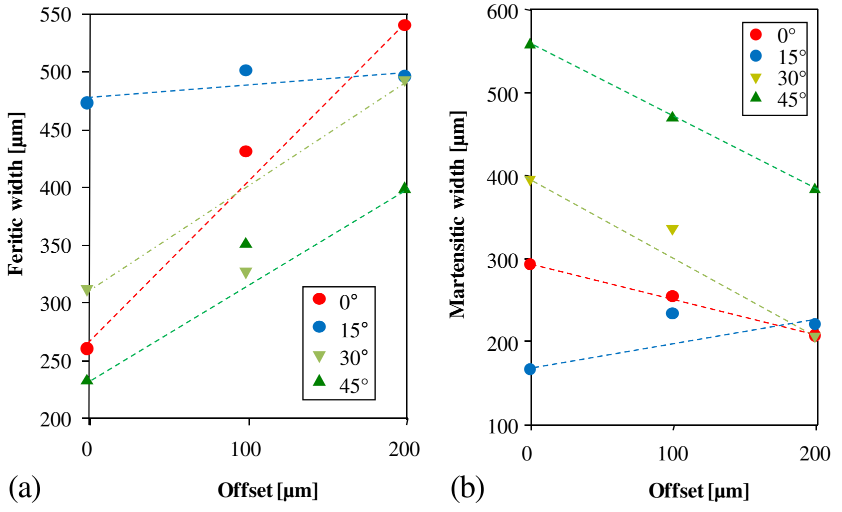

Fig. 5 Measurement of **a** ferritic width and **b** martensitic width for different offset positions and different incident angles. The *dashed lines* are guide to show the trend

where MR is the melting ratio, A_F is the area of ferrite, and A_M is the area of martensite. In the perspective of reducing the incidence of crack formation up to a less dangerous value for the strength of the weld, a more favorable configuration provides larger ferritic area, resulting in higher melting ratio.

This calculation implies the hypothesis of a homogeneous mixing of the two dissimilar steels in the melt pool. As a matter of fact, the melting process is associated with the formation of convective flows [23] (especially Marangoni flows). In case of weld of different steels, this induces a chemical composition homogenization of the melting pool volume. Obviously, some nonhomogeneity could be present, especially in the regions close to the HAZ, but their effects on weld properties are proportional to their extensions, thus almost negligible with respect to the melting pool volume.

Positioning the focal point at the material interface, avoiding any possible misalignment, is extremely important for the described experimental setup. This is obtained by a specifically conceived sharp-pointed jig which is mounted on the optical head and allows for positioning by real contact the head at the material interface at the exact focal distance.

2.2 Experimental procedures

Specimens are clamped and centered in a chuck providing the rotational speed. They are then welded circularly in a butt joint configuration using a continuous wave Rofin fiber laser (maximum power 1 kW). The optical system consisted of a 0.4-mm fiber and two lenses of 200-mm focal and collimate lengths which enable to deliver the laser with a minimum focal spot

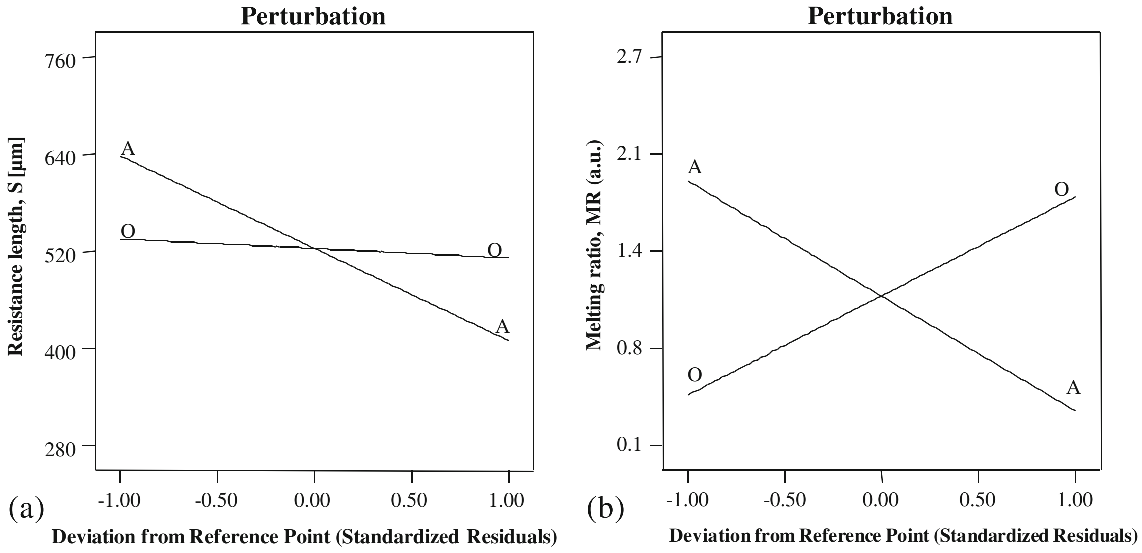

Fig. 6 Perturbation plots showing effects of all factors on **a** resistance length and **b** melting ratio

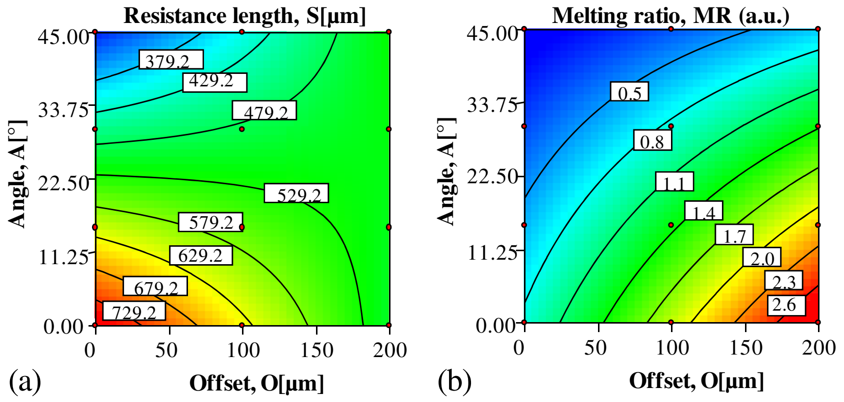

Fig. 7 Contour graphs showing the interaction effects of *O* and *A* on **a** resistance length and **b** melting ratio

diameter of 0.4 mm. The technical details of the employed laser welding process are shown in Table 2.

During experimentation, *O* and *A* are selected as process input variables for the laser welding based on statistical factorial experimental design with full replication. Table 3 shows the experimental conditions, laser welding input variables, and design levels used at a glance. The working range for the incident angle is brought to the upper limit of 45°, for which the highest reflection is expected, while only three steps are hypothesized for the offset, *O*. This is done to avoid insufficient melt of the martensitic steel, as testified by a preliminary set of experiments conducted with O=300 μm.

General full factorial design is utilized as a statistical DOE technique. Full factorial DOE technique relates the welding input parameters to each of the two output responses of the weld (resistance length and melting ratio). Later, the process factors are used as input parameters to develop a mathematical model which links them to the ultimate shear strength of the performed welds. Analysis of variance (ANOVA) and other adequacy measures are used to measure the correctness of the models developed and their significant linear and interaction model terms. Table 4 shows the measurement of the averaged value of response parameters for different laser welding conditions.

Argon is used as shielding gas with a constant flow rate of 6 l/min to protect weld surface from oxidation and suppresses the generation of plasma during welding. A standard ultrasound washing procedure is followed to clean, cool, and dry the specimens. The experimental setup for laser welding system is shown in Fig. 2a.

2.3 Weld bead characterization

After welding, seam cross sections are prepared by cutting the samples axially using SampleMet II (Beuhler, IL) model abrasive cutter. The sectioned samples are mounted, polished, and chemically etched by immersion in Vilella reagent for microstructural characterization. Leica IM500 software, incorporated in an optical microscope (Leica MZ125), is used to measure resistance length, martensitic and ferritic weld width, and the area of ferrite and martensite needed to calculate the melting ratio according to Eq. 1.

Experiments are replicated six times for each welding combination (*A*; *O*) to produce three specimens to be cut for metallographic analysis and three for the mechanical characterization of the weld (see Sect. 2.4). Figure 3 reports the typical cross section at the reference position and at the extreme values of the parameter tested range.

The guidance on quality levels for imperfections given in ISO 13919-1:1996 [21] is followed to ensure the desired weld quality in terms of surface cracking. At this point, each welded specimen is visually inspected using the optical microscope.

Table 6 Sequential model sum of squares for resistance length model

Source	Sum of squares	*df*	Mean square	*F* value	*P* value Prob>*F*	
Mean	3.292E+006	1	3.292E+006	–	–	–
Linear	88148.54	2	44074.27	4.11	0.0538	
2FI	64400.62	1	64400.62	16.10	0.0039	Suggested
Quadratic	13236.46	2	6618.23	2.12	0.2017	
Cubic	15963.75	3	5321.25	5.69	0.0936	Aliased
Residual	2806.87	3	935.62	–	–	–
Total	3.476E+006	12	2.897E+005	–	–	–

Table 7 Model summary statistics for resistance length model

Source	Std. dev.	R^2	Adj R^2	Pred R^2	PRESS	
Linear	103.50	0.4776	0.3615	−0.1093	2.047E+005	
2FI	63.25	0.8266	0.7615	0.5788	77734.99	Suggested
Quadratic	55.93	0.8983	0.8135	0.6506	64492.73	
Cubic	30.59	0.9848	0.9442	0.7809	40443.16	Aliased

2.4 Mechanical characterization

Being it impossible to obtain specimens of standard geometry (to be tested in a common shear stress test) from small size components as the ones welded in this study, the mechanical properties of the performed joints are characterized with a push-out test of the internal martensitic shell with respect to the outer one. This test practiced on the entire assembled components allows for the characterization of the whole seam (difference in the geometry may appear during the laser power ramp-up or ramp down). Moreover, the constrained circular configuration of the weld avoids distortions during the test, as it often happens from specimen cut from a pressure vessel (e.g., curvature problems, load misalignment due to the thickness of the shells, etc.).

All welding configurations are then tested to shear stresses under the action of a calibrated press exerting its load on a specifically conceived expeller. The photographic view in Fig. 4a shows the setup for the push-out test in which the weld fails due to the disassembly forces while the model for weld shear failure is sketched in Fig. 4b: the draft shows the surfaces in contact during the test. The load of the press increases quasi-statically, and the maximum value generating the collapse of the joint (the ultimate shear stress) is recorded.

3 Results and discussion

The effects of individual process parameters (incidence angle and offset) on geometrical features of the weld cross sections (resistance length and melting ratio) are plotted by perturbation plots and described in the following sections. To demonstrate the two-factor interaction effects on the same weld bead geometry, contour plots are used. Figure 3 shows typical cross sections and weld profiles in the following: (a) reference position and (b) the extreme values of the incidence angle and the offset at the same time. It is possible to see that, according to the weld design strategy described in Sect. 2.1, the control of the weld position by a proper selection of input parameters allows to vary the melting ratio in favor of martensite or ferrite.

3.1 Visual inspection of weld quality

The reference position welding configuration shows sporadic superficial defects whose dimensions can be considered acceptable according to the ISO 13919-1 standard (grade 1). Results of weld seam inspection are reported in Table 5 as function of the analyzed weld geometry configurations. Results show that increasing the incident angle induces higher ISO 13919 standard numbers, but increasing the offset decreases the number and dimensions of microcracks. This means that the presence of microcracks is mainly driven by the relative volume fraction of AISI 440C and AISI 430F steels in the welds. Higher martensitic volume fraction induces higher susceptibility to surface crack formation (tens of microns length). In fact, microcracks are found to develop always on the boundary of the weld seam with AISI 440C.

3.2 Ferritic and martensitic width (W_F and W_M)

In the reference position, the width at the free surface is nearly the same for the two materials as it is possible to notice also in Fig. 3a. Melt pool width on the ferritic side is slightly smaller

Table 8 Sequential model sum of squares for melting ratio model

Source	Sum of squares	*df*	Mean square	*F* value	*P* value Prob>*F*	
Mean	14.52	1	14.52			
Linear	7.46	2	3.73	44.42	<0.0001	
2FI	0.55	1	0.55	21.67	0.0016	Suggested
Quadratic	7.083E−003	2	3.542E−003	0.11	0.8993	
Cubic	0.13	3	0.042	1.75	0.3278	Aliased
Residual	0.071	3	0.024	–	–	–
Total	22.74	12	1.90	–	–	–

Table 9 Model summary statistics for melting ratio model

Source	Std. dev.	R^2	Adj R^2	Pred R^2	PRESS	
Linear	0.29	0.9080	0.8876	0.8032	1.62	
2FI	0.16	0.9752	0.9659	0.9420	0.48	Suggested
Quadratic	0.18	0.9761	0.9561	0.8979	0.84	
Cubic	0.15	0.9913	0.9681	0.8519	1.22	Aliased

due to the higher thermal conductivity of AISI 430F with respect to AISI 440C (25 and 15 W m^{-1} K^{-1}, respectively): the ED transferred to the material can be easier conducted away by the outer shell. This thermal loss makes heat conduction anisotropic in the present case. The effect of increasing the offset on the melt pool width on both sides (averaged values) is shown in Fig. 5 for different incident angles. Increasing the offset obviously results in an almost linear increment of ferritic width for all the incident angles, conversely for the martensitic one. Increasing the incident angle has an opposite effect which compensates the asymmetry generated by the use of large values of the offset, as hypothesized in Sect. 2.1.

The base metal microstructures are typically composed by a martensitic matrix with presence of primary and secondary Cr carbides for the AISI 440C and a ferritic matrix with elongated MnS particles for AISI 430F steel.

3.3 Effects of process parameters

To compare the effects of all the process parameters at the center point in the design space, the perturbation plot is drawn and is shown in Fig. 6a, b. The results suggest that incidence angle of laser has the most significant negative impact on both the resistance length and MR. For melting ratio, an opposite phenomenon of the same entity is observed for the offset: MR increases linearly with the increase of offset, and the two linear dependencies are found to be symmetric with respect to the center point. On the other hand, the resistance length is not remarkably affected by the change of offset, at least in the tested range.

Figure 7a shows the contour plot for resistance length as a function of interaction between offset and angle. For the initial two levels of *A* (0° and 15°), *S* increases with the increase of *O* while the opposite phenomena are observed for the other two levels of *A*.

Contour plots as shown in Fig. 7b demonstrate the fact that interactions of higher offset and lower incidence angle of laser cause higher melting ratio. In the reference position, the averaged melting ratio on the three weld specimens results MR=0.8: this value is lower than one which theoretically represents a condition of symmetry with respect to the interface between the two materials. Actually, the ferritic area results smaller than the martensitic one for all the three samples tested in the same condition. This phenomenon can be traced back to the already mentioned higher thermal conductivity of AISI 430F which favors heat conduction away from the irradiated area. As a result, the melt pool develops more on the AISI 440C area and makes this material, which is also characterized by a much more brittle microstructure, more susceptible to cracking. Thus, it should be taken into account that even in a symmetric configuration, like the reference position, the weld pool develops in asymmetric way due to the different thermal properties of the two dissimilar metals. MR increases almost linearly with the offset for each incidence angle: it especially increases faster for 0° and 15° for which the percentage of melt ferrite more than doubles. For the higher values of *A*, the direction of the beam axis, pointing to the martensitic steel, compensates the effect of the offset and the rate of growth of the ferritic area is less pronounced.

3.4 Development of mathematical models

At this stage, the fit summary in the Design-Expert software V7 is used to select the models that best describe the response factors. The fit summary includes sequential model sum squares to select the highest order polynomial where additional terms are significant and the model is not aliased. In addition, model summary statistics of the fit summary focuses on the model that maximizes adjusted R^2 and predicted R^2 values. The sequential F test and lack-of-fit test are carried out using the same statistical software package to check if the regression

Table 10 ANOVA table for resistance length 2FI model

Source	Sum of squares	*df*	Mean square	*F* value	*P* value Prob>*F*	
Model	1.525E+005	3	50849.72	12.71	0.0021	Significant
O	1128.13	1	1128.13	0.28	0.6098	
A	87020.42	1	87020.42	21.75	0.0016	
OA	64400.62	1	64400.62	16.10	0.0039	
Residual	32007.08	8	4000.89			
Cor total	1.846E+005	11				

R^2 =0.8266, adj R^2 =0.7615, pred R^2 =0.5788, adeq precision=12.85

Table 11 ANOVA table for melting ratio 2FI model

Source	Sum of squares	*df*	Mean square	*F* value	*P* value Prob>*F*	
Model	8.02	3	2.67	104.87	<0.0001	Significant
O	3.51	1	3.51	137.81	<0.0001	–
A	3.95	1	3.95	155.13	<0.0001	–
OA	0.55	1	0.55	21.67	0.0016	–
Residual	0.20	8	0.025	–	–	–
Cor total	8.22	11	–	–	–	–

R^2 =0.9752, adj R^2 =0.9659, pred R^2 =0.9420, adeq precision=31.088

model is significant and to find out the significant model terms of the developed models as well. The stepwise regression method is also applied to eliminate the insignificant model terms automatically.

Suitable response models for the response factors are selected based on the fit summaries. From fit summary output of the measured responses shown in Tables 6, 7, 8, and 9, it is evident that two-factor interaction (2FI) models are statistically recommended for further analyses of both the resistance length and melting ratio.

The test for significance of the regression models and the test for significance on individual model coefficients are performed using the same statistical package. By selecting the stepwise regression method that eliminates the insignificant model terms automatically, the resulting ANOVAs in Tables 10 and 11 for the selected models summarize the ANOVA of each response and illustrate its significant model terms as well. The aforestated tables demonstrate that calculated Fisher's "Model-F" and "Model-P" values are, respectively, 12.71 and 0.0021 for resistance length's 2FI model and 104.87 and <0.0001 for melting ratio 2FI model. These Model-F and Model-P values imply that the selected models are highly significant and there is only 0.21 % and a less than 0.01 % chance that these large Model-*F* values could occur due to noise. The associated *P* value is also used to estimate whether *F* is large enough to indicate statistical significance. If *P* value is lower than 0.05, it indicates that the model is statistically significant as stated by Zulkali et al. [24].

Tables 10 and 11 also show other adequacy measures, e.g., R^2, adjusted R^2, and predicted R^2 values. All the adequacy measures are in logical agreement and indicate significant relationships. Moreover, adequate precision compares range of predicted value at the design points to average prediction error. The adequate precision ratios in all cases are dramatically greater than 4 indicating adequate model discrimination. Again, the ANOVA tables for the resistance length model and melting ratio model show that all two linear terms, i.e., offset and laser incident angle and two-factor interactions (2FI) of offset-angle (*O*-*A*), are significant model terms. From the results shown in Tables 6, 7, 8, 9, 10, and 11, it is, therefore, apparent that the developed statistical models for predicting resistance length and melting ratio are fairly accurate and can be of following forms:

1. Resistance length, $S=523.75-11.87\times O-114.25\times A+120.37\times O\times A$

Fig. 8 Normal probability plot for **a** resistance length and **b** melting ratio

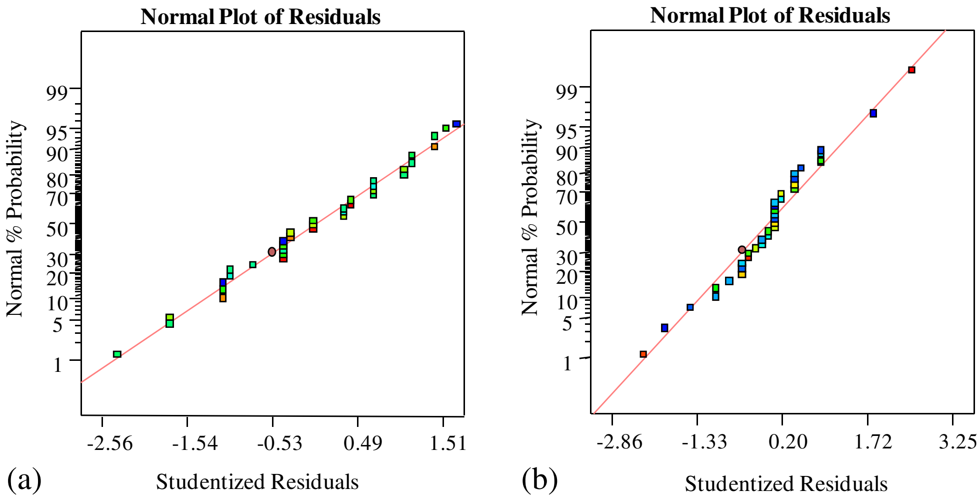

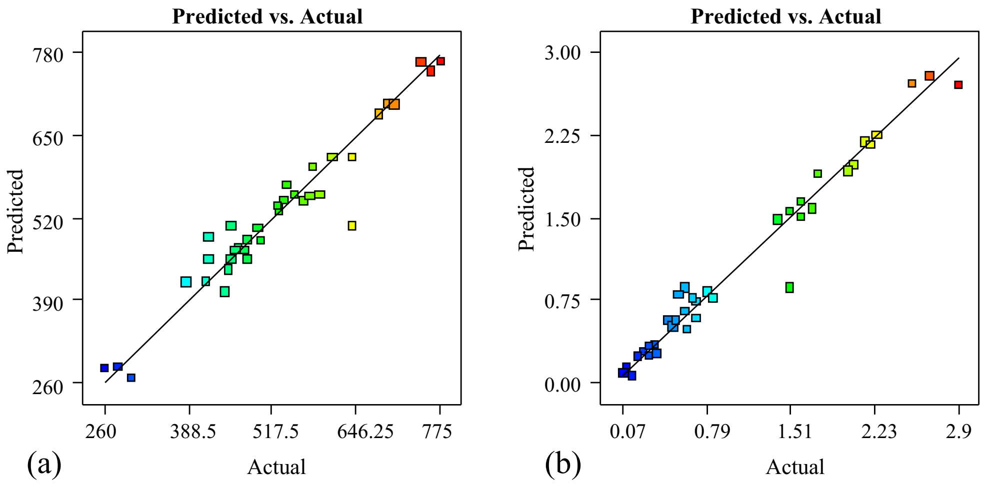

Fig. 9 Scatter diagrams of **a** resistance length and **b** melting ratio

2. Melting ratio, $MR = 1.1 + 0.66 \times O – 0.77 \times A - 0.35 \times O \times A$

Normality of residual data and amount of residuals in prediction are then checked to ensure statistical validation of the developed models. The normality of data is verified by plotting the normal probability plot (NPP) of residuals. The residual is the difference between observed and predicted values (or fitted value) obtained from the regression model. The data set is normally distributed if the points on the plot fall fairly close to the straight line. The NPPs of residual values for weld resistance length and melting ratio are depicted in Fig. 8a, b, respectively. The experimental points are reasonably aligned with predicted or fitted points suggesting the normality of data. This is an implication that empirical distribution of residual data is well compared with a normal distribution having the same mean and variance.

Figure 9a, b shows the relationships between the actual and predicted values of weld resistance length and melting ratio. Since the points plotted are close to and around the diagonal line, the difference between the predicted and actual values for each point can be considered to be minimal. It is also an indication that the statistical models for prediction are adequate and predicted results are in good agreement with the measured data.

Table 12 Summary of results of investigated parameters

Welding configuration	Averaged melting ratio, MR (a.u.)	Carbon in melting pool (%)	Averaged resistance length, *S* (μm)	Surface cracks[a]	Averaged USF (*N*)
1	0.8	0.66	760	1	4900
2	2.0	0.45	695	0	4380
3	2.7	0.38	465	0	4180
4	0.5	0.77	535	3	3825
5	1.6	0.49	610	0	4200
6	2.2	0.43	450	0	4020
7	0.3	0.87	480	3	3550
8	0.6	0.73	550	2	3940
9	1.5	0.51	590	0	4540
10	0.1	1.01	280	3	2710
11	0.3	0.87	415	3	3650
12	0.6	0.73	455	2	4090

All data refer to the average value of three specimens. Values are attributed according to ISO 13919-1:1996 [17], after inspection on the three samples for each configuration

[a] 0=no defects, 1=exist but acceptable, 2–3=not acceptable

3.5 Ultimate shear force

The value of the ultimate force making the weld collapsing under shear stresses, averaged for the three tested samples, is reported in Table 12 along with all the other investigated parameters (*S*, MR, crack grade). All failure data reported in Table 12 (under the column "Averaged ultimate shear force (USF)") are related to a brittle fracture of the weld. The applied load increases quasi-statically with increasing the application time up to the moment in which the fracture propagates drastically over the 360° detaching the two components.

The averaged MR gives an indication of the carbon content of the fusion zone (also reported in the table), where the chemical composition is the average between the two base steels weighted for their volume fraction. This is because, as reported in Table 1, the other main element (chromium, manganese, and silicon) concentrations are almost the same for the two welded steels; thus, the properties of the melting pool are driven by the carbon content. It ranges between 0.4 and 1 % for the highest and lowest measured MR values, respectively.

According to the literature [15, 25], the USF linearly depends on the dimension of the resistance length. The highest

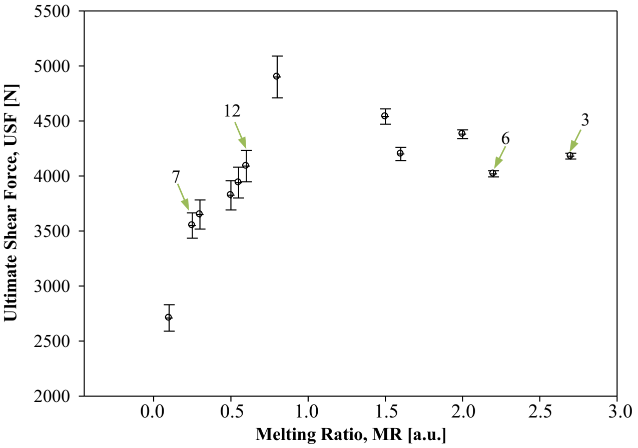

Fig. 10 Ultimate shear force of the fusion zone as a function of melting ratio

USF is then obtained in the reference position for which the resistance length has the highest value within the tested range.

Nevertheless, a second important effect on USF can be also noticed referring to those configurations having a nearly same resistance length but different melting ratio. Considering only the linear dependence of USF on the resistance length, those configurations having a similar S (±10 μm) should break under a similar load. Conversely, Table 12 shows that configurations 3 and 6 result in a sensible higher USF in respect to 7 and 12 for which the percentage of martensitic material in the melt pool is higher.

Figure 10 representing the behavior of USF as a function of the melting ratio obviously includes also the dependence on S. In order to give evidence on how the melting ratio influences the USF, couples of welding configurations having the same S but different MR have to be considered. As an example, welding configuration numbers 3 and 6 (see Table 12) with MR=(2.7–2.2), respectively, and S=(450–460) μm can be compared to numbers 7 and 12 (obtained with large A): S=(450–480 μm) but opposite MR=(0.3–0.6) as indicated by arrows in Fig. 10. Measured data reveal that increasing the volume fraction of the ferritic stainless steel in the melt pool has beneficial aspects on the ultimate shear strength. Also, data dispersion (with respect to the averaged value reported in Table 12) decreases with increasing MR, making the failure mode more predictable. This means that the prevailing effect is the decreased brittleness of the weld by decreasing its carbon content. In fact, high carbon content in the melt pool not only increases the crack susceptibility but also lowers the USF.

Experimental results suggest the use of welding configurations generating MR ≥1.5 to obtain a crack-free surface (grade 0 according to the ISO 13919-1 standard) and to ensure high and well-reproducible USF.

An attempt to link mathematically the USF to the parameters which determine the welding configuration is developed by means of the full factorial DOE.

$$\mathrm{USF} = 1408.18 + 4778.52 \times O + 940.85 \times A - 1562.99 \times O \times A$$

The NPP of residual values for USF is depicted in Fig. 11. The experimental points are reasonably aligned with predicted or fitted points suggesting the normality of data. This is an implication that empirical distribution of residual data is well compared with a normal distribution having the same mean and variance.

Figure 12 shows the relationships between the actual and predicted values of weld USF. Since the points plotted are close to and around the diagonal line, the difference between the predicted and actual values for each point can be

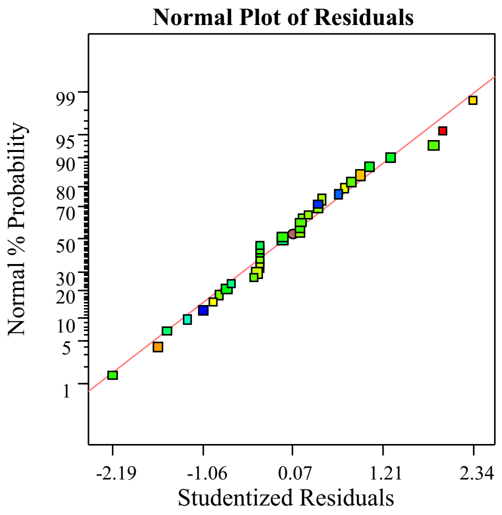

Fig. 11 Normal probability plot weld USF

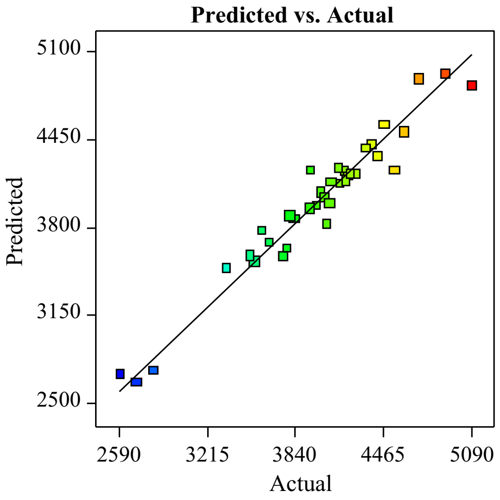

Fig. 12 Scatter diagram of USF

considered to be minimal. From Fig. 12, it is clear that the predicted results are in good agreement with the measured data for USF.

4 Conclusions

Ferritic AISI 430F and martensitic AISI 440C stainless steel shells have been laser welded in constrained butt configuration. The effects of different combination of incident angles and offsets have been studied, analyzing the following parameters of the fusion zone: cross-sectional geometry (resistance length and width at the free surface), melting ratio between the dissimilar steels, presence of surface cracks and relative dimensions, and ultimate shear strength of the welds. For the laser system, weld joint type, and the limits of laser parameters considered in this study, the following points can be concluded:

The presence of surface cracks is more relevant when the melting ratio is lower than 0.8 (reference position). This is more evident with incident angles of 30° and 45°, although some mitigations could be obtained by increasing, at the same time, the offset value. It was shown that the welding configuration controls the geometry of the weld and the mixing between the dissimilar steels which influences strength and brittleness of the seam.

Both resistance length and melting ratio can be readily linked to laser offset and incidence angle at the shell interface by using a linear regression over the experimental data. Remarkably, the melting ratio is a good indicator of the carbon content on the fusion zone and the critical value MR=1.5 is related to carbon content in the fusion zone of about 0.5 %.

Well-reproducible USF in the range of 4.5–4 kN can be obtained with welding configurations generating MR $\geq$1.5 with an almost negligible incidence of surface cracks (grade 0 according to the ISO 13919-1 standard).

It was proved that the ultimate shear strength is not only linearly dependent on the resistance length but also susceptible to the micromechanical properties of fusion zone (especially brittleness) and, thus, to the melting ratio.

Measured data revealed that it is possible to find an empirical relationship between the shear strength of the weld and the configuration adopted during experiments by using full factorial DOE.

These conclusions pinpointed for the welding conditions under investigation can be easily extended to a broader range of weld designs under the limiting condition that the formation of the weld bead is conduction dominated and plasma formation is not considered.

Acknowledgements Maria Carmela Fierro, laser-welding expert at Continental Automotive Italy s.p.a., is sincerely acknowledged for providing means and facilities needed to carry out the experimental phase.

References

1. Messler WRJ (2004) Joining of metals, alloys, and intermetallics. Joi Mater Struct pp. 535–582
2. Wenyong W, Shengsun H, Shen J (2015) Microstructure, mechanical properties and corrosion behavior of laser welded dissimilar joints between ferritic stainless steel and carbon steel. Mater Des 65:855–861
3. Phanikumar G, Manjini S, Dutta P, Mazumder J, Chattopadhyay K (2005) Characterization of a continuous CO_2 laser-welded Fe-Cu dissimilar couple. Metall Mater Trans A 36A:2137–2147
4. Sun Z, Ion JC (1995) Laser welding of dissimilar metal combinations. J Mater Sci 30:4205–4214
5. Duley WW (1999) Laser welding. Wiley, New York
6. Vaidya WV, Horstmann M, Ventzke V, Petrovski B, Kocak M, Kocik R, Tempus G (2010) Improving interfacial properties of a laser beam welded dissimilar joint of aluminium AA6056 and titanium Ti6Al4V for aeronautical applications. J Mater Sci 45:6242–6254
7. Chen L, Zhou L, Tang C, Huang W, Wang C, Hu X, Wang J, Yan F, Wang X, Jiang Z, Shao X (2014) Study of laser butt welding of SUS301L stainless steel and welding joint analysis. Int J Adv Manuf Technol 73:1695–1704
8. Caiazzo F, Alfieri V, Sergi V, Schipani A, Cinque S (2013) Dissimilar autogenous disk-laser welding of Haynes 188 and Inconel 718 superalloys for aerospace applications. Int J Adv Manuf Technol 68:1809–1820
9. Gao M, Wang ZM, Li XY, Zeng XY (2012) Laser keyhole welding of dissimilar Ti-6Al-4V titanium alloy to AZ31B magnesium alloy. Metall Mater Trans A 43A:163–172
10. Berretta JR, de Rossi W, Neves MDM, de Almeida IA, Junior NDV (2007) Pulsed Nd:YAG laser welding of AISI 304 to AISI 420 stainless steels. Opt Lasers Eng 45:960–966
11. Liao YC, Yu MH (2007) Effects of laser beam energy and incident angle on the pulse laser welding of stainless steel thin sheet. J Mater Process Technol 190:102–108
12. Benyounis KY, Olabi AG (2008) Optimization of different welding processes using statistical and numerical approaches—a reference guide. Adv Eng Softw 39:483–96
13. Anawa EM, Olabi AG (2008) Optimization of tensile strength of ferritic/austenitic laser-welded components. Opt Lasers Eng 46:571–577
14. Ruggiero A, Tricarico L, Olabi LG, Benyounis KY (2011) Weld-bead profile and costs optimisation of the CO2 dissimilar laser welding process of low carbon steel and austenitic steel AISI316. Opt Laser Technol 43:82–90
15. Khan MMA, Romoli L, Fiaschi M, Dini G, Sarri F (2012) Multiresponse optimization of laser welding of stainless steels in a constrained fillet joint configuration using RSM. Int J Adv Manuf Technol 62:587–603
16. Marashi P, Pouranvari M, Amirabdollahian S, Abedi A, Goodarzi M (2008) Microstructure and failure behavior of dissimilar resistance spot welds between low carbon galvanized and austenitic stainless steels. Mater Sci Eng A 480:175–180
17. Torkamany MJ, Sabbaghzadeh J, Hamedi MJ (2012) Effect of laser welding mode on the microstructure and mechanical performance of dissimilar laser spot welds between low carbon and austenitic stainless steels. Mater Des 34:666–672

18. Rossini M, Russo Spena P, Cortese L, Matteis P, Firrao D (2015) Investigation on dissimilar laser welding of advanced high strength steel sheets for the automotive industry. Mater Sci Eng A 628:288–296
19. Baghjari SH, AkbariMousavi SAA (2014) Experimental investigation on dissimilar pulsed Nd:YAG laser welding of AISI 420 stainless steel to kovar alloy. Mater Des 57:128–134
20. Franco A, Romoli L, Musacchio A (2014) Modelling for predicting seam geometry in laser beam welding of stainless steel. Int J Therm Sci 79:194–205
21. ISO 13919-1:1996 Welding—electron and laser-beam welded joints—guidance on quality levels for imperfections—part 1: steel (reviewed in 2011).
22. Serizawa H, Mori D, Shirai Y, Ogiwara H, Mori H (2013) Weldability of dissimilar joint between F82H and SUS316L under fiber laser welding. Fusion Eng Des 88(9-10):2466–2470
23. Rai R, Elmer JW, Palmer TA, DebRoy T (2007) Heat transfer and fluid flow during keyhole mode laser welding of tantalum, Ti–6Al–4V, 304L stainless steel and vanadium. J Phys D Appl Phys 40: 5753–5766
24. Zulkali MMD, Ahmad AL, Norulakmal NH (2006) Oryza sativa L. husk as heavy metal adsorbent: optimization with lead as model solution. Bioresour Technol 97:21–25
25. Khan MMA, Romoli L, Fiaschi M, Dini G, Sarri F (2012) Laser beam welding of dissimilar stainless steels in a fillet joint configuration. J Mater Proc Technol 212:856–867